PAPER

Impurity transport and divertor retention in Ar and N seeded SOLPS 5.0 simulations for ASDEX Upgrade

OPEN ACCESS
IOP Publishing
Plasma Physics and Controlled Fusion
Plasma Phys. Control. Fusion **62** (2020) 085013 (16pp)
https://doi.org/10.1088/1361-6587/ab9b00

Impurity transport and divertor retention in Ar and N seeded SOLPS 5.0 simulations for ASDEX Upgrade

F Hitzler[1,2], M Wischmeier[1], F Reimold[3], D P Coster[1] and the ASDEX Upgrade Team

[1] Max-Planck-Institut für Plasmaphysik, 85748 Garching bei München, Germany
[2] Physik-Department E28, Technische Universität München, 85747 Garching, Germany
[3] Max-Planck-Institut für Plasmaphysik, 17491 Greifswald, Germany

E-mail: ferdinand.hitzler@ipp.mpg.de

Received 21 January 2020, revised 25 May 2020
Accepted for publication 9 June 2020
Published 13 July 2020

Abstract

Impurity seeding will be an important tool to reduce the peak power loads and temperatures at the divertor targets in future tokamak devices. To improve the physics understanding and provide predictive capabilities for the impact of impurities on the plasma, different impurity species have to be investigated and compared to each other. For this purpose SOLPS 5.0 simulations of argon (Ar) and nitrogen (N) seeded H-mode plasmas for ASDEX Upgrade have been performed. The (purely numerical) investigations extend previous studies dedicated to impurity transport and to the divertor impurity retention. An analysis of mixed Ar and N impurity seeding reveals that a trade-off between pedestal top temperature drop and fuel dilution can be achieved by an adjustment of the impurity mixture. Due to the impact of the impurities on the temperatures, the impurity seeding reduces the main ion ionization rates in the divertor regions, and therefore, the ion particle sources. Accordingly, this modification of the particle sources results in a main ion background flow inversion at higher seeding levels, which also strongly affects the impurity flow patterns. This mechanism explains a modification of the impurity density distribution at higher seeding levels, where Ar impurities are observed to be redistributed from the outer to the inner divertor. A less pronounced effect is observed for N, which can be explained by the radiation efficiency. The divertor impurity retention is determined by the relative positions of the ionization front of the neutral impurities and the impurity stagnation point. The impact of impurity seeding on the stagnation point position is studied in detail for the first time. Under the investigated conditions, decreasing the target temperature (i.e. increasing impurity seeding) always results in a reduction of the divertor impurity retention. This is a critical result making power exhaust even more challenging.

Keywords: tokamak, SOLPS simulation, impurity seeding, impurity transport, divertor retention

(Some figures may appear in colour only in the online journal)

1. Introduction

For the operation of a next-step tokamak device, handling power exhaust will be a key challenge. In an unmitigated scenario the foreseen stationary material limits of $5-10\,\mathrm{MW\ m^{-2}}$ for the perpendicular target power loads and 5 eV for the target temperatures will easily be exceeded [1–6]. As a consequence severe damage of plasma facing components and erosion of target material can occur. Therefore, impurity seeding is required, which leads to radiative power dissipation and reduces the temperatures at and power loads to the divertor target plates. In order to find an impurity seeding recipe which provides sufficient power dissipation and, at

the same time, ensures a minimal detrimental impact on the confined plasma and the burn conditions, different impurity species and their impact on the plasma have to be investigated and compared carefully. A mixture of different impurity species can be considered to benefit from several impurities and their characteristic properties at the same time.

Several experiments on different experimental devices are dedicated to the investigation of the impact of impurities on the divertor operation and plasma performance [6–22]. Moderate N seeding is routinely applied in ASDEX Upgrade to reduce the target power loads [23], and also several other impurity species (like, e.g. Ar, Ne, Kr) have been investigated in various impurity seeding experiments (see, e.g. [6, 19]). In these experiments N radiates strongly in the divertor region, while Ar predominantly radiates in the core [6]. Even though differences in the divertor enrichment (defined as the ratio of the impurity concentration in the divertor region to the concentration in the core, $E := c_{\mathrm{div}}/c_{\mathrm{core}}$) can affect this inequality, the differences between N and Ar are mainly caused by the radiation efficiency of the impurity species. The power $P_{\mathrm{rad},z}$ radiated by an impurity can be expressed as the product of the impurity density n_z, the radiation efficiency L_z, and the electron density n_{e}:

$$P_{\mathrm{rad},z} = n_z \cdot L_z \cdot n_{\mathrm{e}}. \tag{1}$$

In coronal equilibrium the radiation efficiency L_z can be derived from atomic databases [24, 25]. The radiation efficiency varies considerably for different impurity species and has a strong temperature dependence. Ar is characterized by a higher radiation efficiency compared to N at high temperatures, i.e. especially in the core region. Only at temperatures below 5 eV the radiation efficiency of N exceeds that of Ar. In the experiment and also in the SOLPS 5.0 simulations, the effective radiation efficiencies are enhanced due to impurity transport which leads to a deviation from the coronal equilibrium [6]. Comparing the effective radiation efficiencies obtained in the simulations in this work to [6], one can estimate the so-called *non-equilibrium parameter* (described in [26]) to be roughly in the order of $n_{\mathrm{e}}\tau \approx 10^{20} - 10^{21}\,\mathrm{m}^{-3}\mathrm{ms}$, which corresponds to a characteristic residence time around $\tau \approx 1 - 10$ ms.

It is also reported in [6] that a considerable energy confinement improvement is observed with N seeding and a moderate improvement with Ar, which is related to a better pedestal performance. However, at the same time the fuel dilution caused by the impurity accumulation in the core will also result in a reduced fusion rate in future fusion devices and should therefore be limited [27]. It also has to be taken into account that in a larger device, as anticipated for future fusion power plants, predictions suggest that divertor radiation alone will not be sufficient to handle the power exhaust and it will be necessary to have a significant amount of additional radiation within the closed flux surfaces [4, 28]. In such a scenario, higher Z species (like Ar) might be required, which also cause less fuel dilution at similar levels of core radiation [25].

One major drawback of experimental analyses is the lack of measurability of certain plasma parameters, or insufficient measurement precision (like, e.g. for the impurity concentrations in the divertor [29–31]). Therefore, in addition to the experimental investigations, also several numerical studies are dedicated to power exhaust and impurity seeding [32–41]. These studies cover different issues, like comparisons of the radiative properties of different impurity species in linear devices [33] and in tokamaks [34], the divertor impurity retention [36], alternative divertor configurations [37–39] and also predictive modeling for ITER [40].

In this work N and Ar seeding under ASDEX Upgrade H-mode conditions is investigated via SOLPS 5.0 modeling [42], without activated drift terms. A detailed reproduction of any particular experimental discharge is not attempted. However, the simulations are aimed to provide a guidance for future experimental investigations. The modeling setup is largely based on [35], where pure Ar seeding is investigated. With the addition of N impurities, also mixed impurity seeding is studied in this work. This allows to identify possible synergetic effects of a mixture of low-Z and medium-Z impurities, which are characterized by different radiative properties. In addition to the impact of thermal forces acting on the impurities in the scrape-off layer (SOL), as discussed in [35], it is found that the impurities influence the main ion plasma flows. The resulting feedback on the impurity flow pattern and on the impurity density distribution is self-consistently taken into account and analyzed, extending previous studies. Regarding the divertor impurity retention, the general discussion in [36] is extended by a detailed analysis of the impact of impurity seeding on the impurity stagnation point position, which (together with the neutral impurity ionization front position) determines the divertor retention. This work contributes to an improved physics understanding of impurity transport and the divertor impurity retention, and gives a first modeling based insight into mixed Ar and N seeding on ASDEX Upgrade.

The modeling setup and the numerical investigations are presented in section 2. A discussion of the analysis, including the expected impact of fluid drifts on the presented results is given in section 3 and, finally, a summary is given in section 4.

2. SOLPS 5.0 modeling

SOLPS 5.0 is a code package combining the fluid plasma code B2.5 and the kinetic Monte Carlo neutral code EIRENE [42]. The codes are iteratively coupled via sink and source terms for particles, momentum and energy. B2.5 solves Braginskii-like equations to determine the parallel transport (of particles, momentum and energy), while the perpendicular transport is calculated via a diffusive approach with user-specified transport coefficients. The different charge states of all implemented atomic species are treated separately as individual fluid species. The forces acting on the particles, especially the thermal force and the friction between main ions and impurities are discussed in more detail in section 2.3. Transport of neutral particles (both atoms and molecules) as well as atomic and molecular processes are handled by EIRENE to determine the neutral particle distribution. The set of atomic and molecular processes applied in this work is largely identical to the set

of reactions presented in [43]. In addition to [43], ionization and recombination reactions for N and Ar, as well as molecular dissociation for N_2 are implemented.

2.1. Modeling setup

To provide a guidance for future experimental investigations on mixed impurity seeding, SOLPS 5.0 simulations were performed on the basis of a reference magnetic equilibrium (resulting in the computational mesh shown in figure 1), which was already used for impurity seeding studies previously [35]. The modeling setup from [35] is used as a starting point for the present simulations. This setup is based on the ASDEX Upgrade H-mode discharge #29 256 which was performed at a magnetic field of -2.5 T, a plasma current of 1 MA and a heating power of roughly 14 MW. In the time window considered for the simulations ($3.0-3.3$ s) the deuterium fueling rate was around $2.4\cdot10^{22}\,\mathrm{es}^{-1}$ and an Ar gas puff around $0.5\cdot10^{21}\,\mathrm{es}^{-1}$ was injected. Under these experimental conditions the outer divertor was in a high-recycling regime, while the inner divertor was detached. The modeling setup is chosen in such a way that the experimental profiles of electron density and temperature at the outer midplane are roughly reproduced [35]. For this purpose, the deuterium fueling rate is feedback controlled in the simulations to maintain an electron density at the outer midplane separatrix of $n_{\mathrm{e,sep}} = 2.5\cdot10^{19}\,\mathrm{m}^{-3}$ and the input power (i.e. the power crossing the core boundary of the computational domain) is set to $P_{\mathrm{input}} = 5$ MW to obtain a separatrix temperature around 100 eV, as in the experiment. Note, that with the experimental heating power of 14 MW, this implies a strong core radiation of roughly 9 MW, which is consistent with the experimental observations in ASDEX Upgrade (see, e.g. [6] for two similar discharges). The perpendicular heat and particle transport diffusion coefficients have been adjusted in [35] to reproduce the experimental profile shapes and are kept fixed for all simulations shown in this work. With this approach (i.e. fixed upstream density, input power and transport coefficients) similar upstream parameters are obtained throughout the whole dataset, permitting the comparison between the different simulations. A poloidal variation of the transport coefficients is implemented to account for a ballooning-like asymmetry of the perpendicular transport with an enhanced transport across the separatrix at the outer midplane. For this purpose, the transport coefficients are rescaled in dependence of the local toroidal magnetic field strength B_{t} via a rescaling factor of $0.834\cdot B_{\mathrm{avg}}/B_{\mathrm{t}}$ (where B_{avg} is the average of the total magnetic field strength over the entire computational domain). To allow kinetic corrections if the system approaches low collisionality, electron and ion heat flux limiters and a viscous flux limiter with values of 0.3, 10 and 0.5 are applied, respectively (see [42] for a description). To investigate the impact of impurities on the plasma, different levels of Ar and N seeding of up to $1.8\cdot10^{21}\,\mathrm{es}^{-1}$ are applied (in electron equivalent units, i.e. $\Gamma_{\mathrm{Ar,e}} = 18\Gamma_{\mathrm{Ar,atoms}}$ and $\Gamma_{\mathrm{N,e}} = 7\Gamma_{\mathrm{N,atoms}}$). At seeding levels above $1.8\cdot10^{21}\,\mathrm{es}^{-1}$, resulting in high radiation fractions $P_{\mathrm{rad}}/P_{\mathrm{input}}$ of $\gtrsim 60\,\%$ (considering only the computational domain), the simulations become increasingly unstable and only a few converged cases were obtained. The Ar and N impurities and also the main ions are fully recycled at the outer boundaries of the computational grid. While this assumption of full recycling is well justified for the noble gas Ar, it should be noted, that this is in general not the case for N. It can be expected, that with realistic N recycling (i.e. with wall pumping of up to 10 % of the impinging N flux [44]), higher N seeding levels would be required to obtain similar radiation fractions. At the divertor targets the Bohm-Chodura sheath boundary conditions are enforced. For the neutral pumping of molecules, deuterium atoms and impurities, a cryo pump and a turbo pump are defined (orange surfaces in figure 1) for which albedos of 0.7 and 0.993 are applied, respectively. Differences in the plasma wall interaction between Ar and N, as well as ammonia production are not taken into account and also drifts and neo-classical effects are neglected.

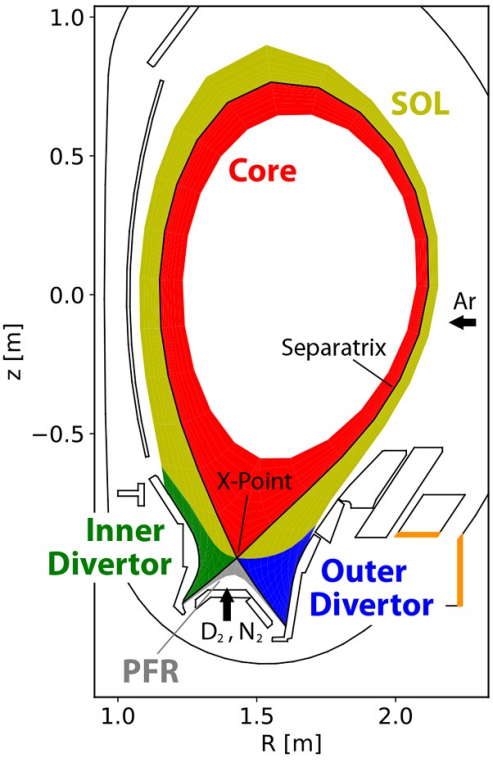

Figure 1. SOLPS 5.0 computational grid based on the magnetic equilibrium of the ASDEX Upgrade shot #29 256. Different colors distinguish the inner and outer divertor regions, the scrape-off layer (SOL), the private flux region (PFR) and the core (which only contains the part of the core covered by the computational domain, i.e. $0.9 \lesssim \rho_{pol} < 1$). The gas puff positions of D_2, N_2 and Ar are indicated by the arrows, and the neutral pumping surfaces are shown in orange.

As convergence criterion for the simulations, steady state conditions of various plasma parameters (like density, temperature, energy and particle fluxes in different regions) are requested. For this purpose a linear trend line is fitted to the time traces and the resulting slope m_X is required to be small compared to the maximum fluctuation of the parameter X, i.e. $m_X \leq 2\cdot10^{-5}\,(\max(X)-\min(X))$. Additionally, the deuterium particle balance (i.e. the discrepancy between

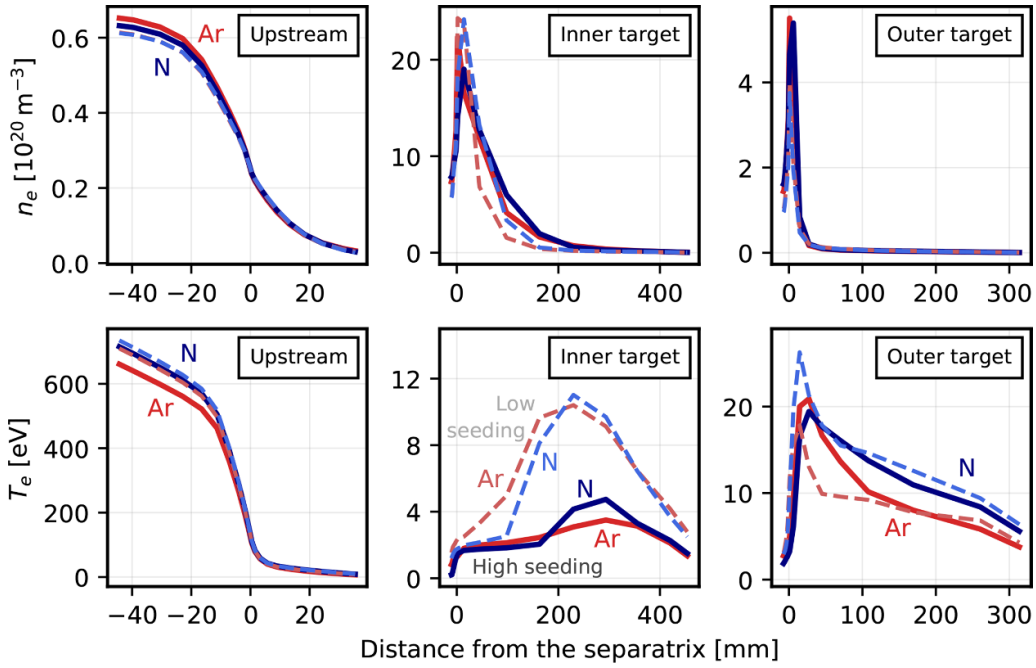

Figure 2. Upstream and target profiles of electron density and temperature for different cases at low and high Ar and N impurity seeding levels: $\Gamma_{Ar} = 1.1 \cdot 10^{21}\,es^{-1}$ (dashed red lines), $\Gamma_{Ar} = 1.5 \cdot 10^{21}\,es^{-1}$ (solid red lines), $\Gamma_N = 0.6 \cdot 10^{21}\,es^{-1}$ (dashed blue lines) and $\Gamma_N = 1.4 \cdot 10^{21}\,es^{-1}$ (solid blue lines).

particle fueling and pumping) is determined, which is observed to be below 5 % in the majority of the simulations.

2.2. *Argon and nitrogen impurity seeding scans*

An overview over the upstream and target profiles of electron density and temperature is shown in figure 2 for two Ar and N seeding cases with low and high seeding level, respectively. Figure 3 shows the evolution of the average impurity densities (i.e. the average over the computational grid cells within the particular region) and the power radiated by the impurities in different regions for the Ar and N impurity seeding seeding scans. The impurity densities steadily increase in all regions with increasing seeding levels. In the Ar seeding scan above a seeding level of $1.22 \cdot 10^{21}\,es^{-1}$ (dotted vertical line in the Ar plots) Ar impurities are redistributed from the outer to the inner divertor. In the following this modification of the impurity density distribution will be referred to as *'density redistribution'* (even though it does not describe an actual time dependent redistribution process, but only a transition between two different steady-state plasma solutions). At higher seeding levels the Ar core density saturates or even begins to decrease slightly, while the Ar core radiation (figure 3, right) continues to increase. The Ar core radiation exceeds the N core radiation by a factor of 2, even though the Ar density in the core is about a factor of 3 lower compared to the N density. This high and continuously increasing Ar core radiation can be explained by the temperature dependence of L_z. The total radiated power summed over the whole computational domain is roughly the same for Ar and N at similar (electron equivalent) impurity seeding levels (with the contributions of the radiation in the SOL and in the PFR not shown in figure 3).

While the electron density at the upstream separatrix position is kept fixed (see section 2.1), the electron density at the core boundary slightly increases at higher seeding levels (not shown here). The electron temperature in different plasma regions and the maximum inner and outer divertor target power loads are shown in figure 4. As expected, the radiative power dissipation leads to a reduction of the temperature and power load in all regions. The strong pedestal top temperature drop caused by the increased Ar core radiation reveals a detrimental impact of Ar on the confined plasma. In comparison, such a strong impact on the pedestal is not observed for N at comparable target conditions.

An overview over the operational space can be provided by plotting the peak target temperature and the peak power load against the pedestal top temperature drop. This is shown in figure 5 for the inner target (left) and the outer target (right). With sufficient impurity seeding it is possible to meet both the temperature and power load constraints at the inner target as well as the power load constraint at the outer target. Only for the peak target temperature at the outer target the 5 eV limit is exceeded in all cases. The best results in terms of pedestal top temperature (i.e. the strongest reduction of the target temperatures and power loads and at the same time the lowest pedestal top temperature drop) are obtained with pure N seeding. On the other hand, the fuel dilution in the confined region has to be limited, as it reduces the maximum achievable fusion rate in a future fusion device. The fuel dilution is defined as the ratio of the main ion species density and the electron density $\frac{n_{D+}}{n_e}$. In the simulations, less fuel dilution is obtained with Ar seeding than with N seeding. This is due to the higher atomic number and the higher Ar radiation efficiency, which results in lower required Ar densities at similar power dissipation levels.

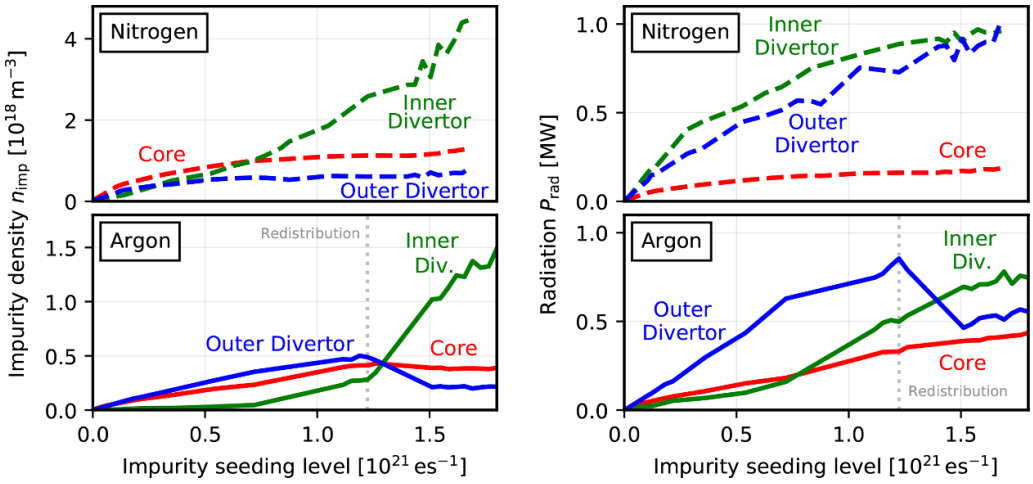

Figure 3. Impurity densities n_{imp} (left) and impurity line radiation P_{rad} (right) for the N seeding scan (top) and the Ar seeding scan (bottom) in different regions (as defined in figure 1). For the densities, the average over the computational grid cells within the particular region is displayed. The vertical dotted lines (here and in the following plots) indicate the position of the *impurity density redistribution* (see text).

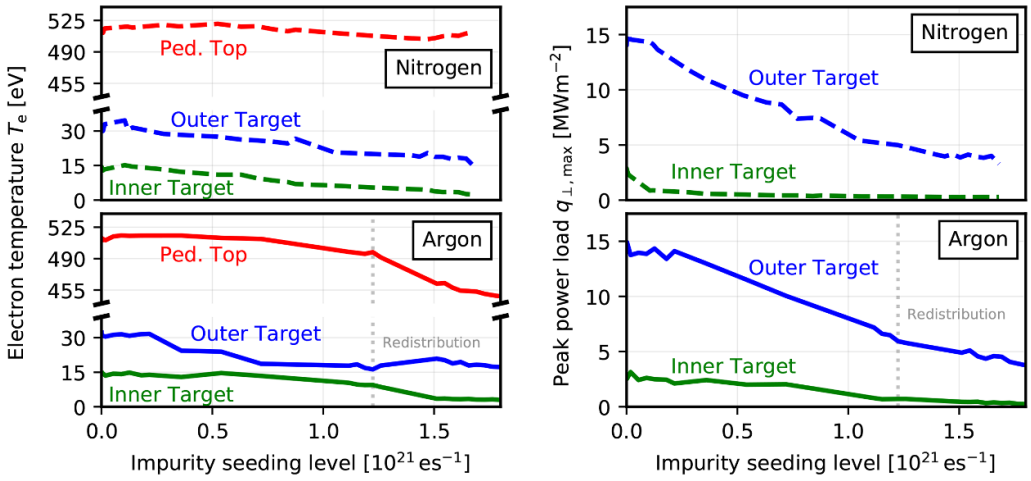

Figure 4. Electron temperature T_{e} in different regions (left) and maximum inner and outer divertor target power loads $q_{\perp,\mathrm{target,max}}$ (right) for N (top) and Ar (bottom). The target values (green, blue) are the peak values at the particular divertor target and the core value (red) is the average over the closed flux surface at the pedestal top position, i.e. at $\rho_{\mathrm{pol}} \approx 0.96$.

In figure 6 the pedestal top temperature is plotted against the fuel dilution (averaged over the closed flux surface at the pedestal top position) for various cases. The mixing of Ar and N impurities at different mixing ratios allows to achieve a trade-off between pedestal top temperature drop and fuel dilution (i.e. a lower impact on the pedestal top temperature with a higher N fraction, or less fuel dilution with a higher Ar fraction). Depending on which of these two parameters is considered to be more critical in a certain plasma scenario, the impurity mixture can be adjusted accordingly.

Finally, figure 7 shows the impurity concentrations $c_{\mathrm{imp}} = \frac{n_{\mathrm{imp}}}{n_{\mathrm{e}}}$ in different regions and the inner and outer divertor enrichment $E = \frac{c_{\mathrm{imp,div}}}{c_{\mathrm{imp,core}}}$, which can be used to assess the impurity retention in the divertor region. At seeding levels below $1.22 \cdot 10^{21}\,\mathrm{es}^{-1}$ Ar is characterized by a high enrichment in the outer divertor. However, at higher seeding levels, the density redistribution results in a strongly reduced Ar enrichment in the outer divertor and an increased enrichment in the inner divertor. A comparable behavior in the N seeding scan is also visible in figure 7, where the N concentration in the inner divertor exceeds that in the outer divertor above a seeding level of $0.9 \cdot 10^{21}\,\mathrm{es}^{-1}$. However, the effect is much less pronounced for N. To understand this behavior and the difference between N and Ar we investigate the impurity transport and the divertor impurity retention in more detail in the next section.

In addition to the impurity concentrations, the ratio of the impurity seeding level (in atoms/s) to the deuterium fueling level $\frac{\Gamma_{\mathrm{imp}}}{\Gamma_{\mathrm{D}^+} + \Gamma_{\mathrm{imp}}}$ is shown in figure 7, left (thin gray lines). In the experiment, this ratio is often used to estimate the impurity concentration in the divertor region, as a direct measurement is often not possible due to strong variations of the plasma parameters along the viewing lines of the diagnostics and insufficient quality of atomic data for spectroscopy [31]. For the present simulations (i.e. under the conditions defined by the modeling setup described above) this estimate agrees reasonably well with the actual divertor impurity concentrations.

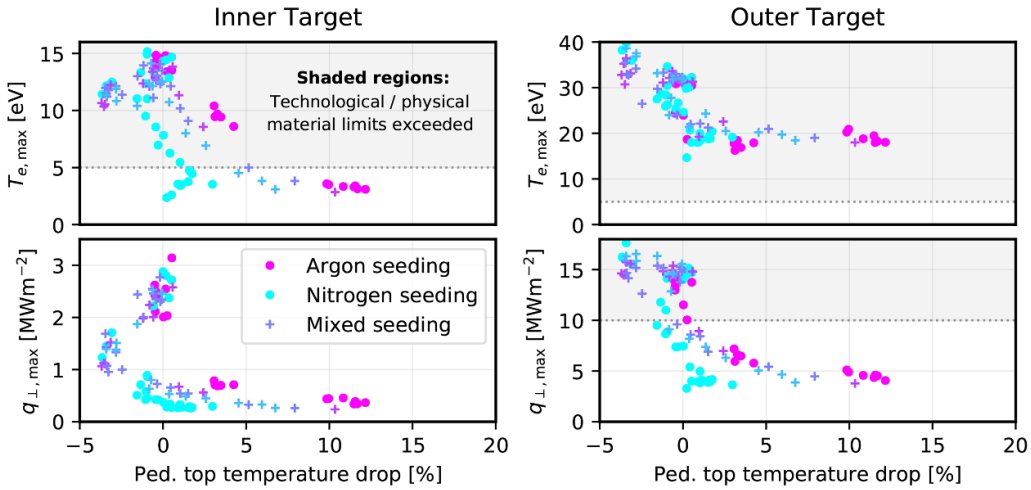

Figure 5. Overview over the operational space showing the peak target temperature and perpendicular power load plotted against the pedestal top temperature drop (compared to the unseeded reference case) for the inner target (left) and for the outer target (right). In addition to the pure Ar and N seeding scans, also mixed seeding cases with mixing ratios of $\Gamma_{Ar}:\Gamma_N = 2:1$, $1:1$ and $1:2$ (in terms of atomic fluxes) are shown. The shaded regions indicate the parameter space in which the material limits of 5 eV and 10 MWm^{-2} are exceeded.

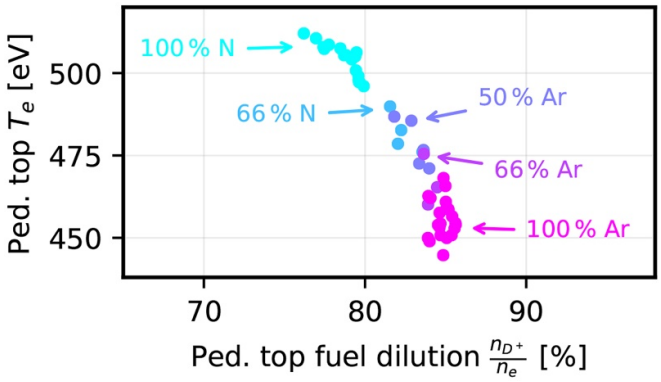

Figure 6. Pedestal top temperature plotted against the fuel dilution averaged over the closed flux surface at the pedestal top position (at $\rho_{pol} \approx 0.96$). Shown are only the cases which satisfy the target material limits as depicted in figure 5 (with the exception of the outer target temperature limit for which no cases with $T_e < 5$ eV are obtained). Different Ar to N mixing ratios are distinguished by the color coding.

However, the estimate cannot differentiate between the inner and outer divertor and, depending on the actual density distribution, it may yield an intermediate value, or it matches either only the inner or only the outer divertor concentration.

In all of the simulations presented above, the deuterium fueling rate was feedback controlled to sustain an upstream separatrix electron density of $n_{e,sep} = 2.5 \cdot 10^{19}\,\mathrm{m}^{-3}$, as described in section 2.1. As it can be seen in figure 8 (left), showing the averaged deuterium fueling rate in the Ar seeding scan, at high seeding levels the deuterium fueling has to be increased considerably (by a factor of 3) to meet this target. This can be understood if one considers that with the power dissipation caused by the impurities, the reaction rate for the ionization of the fuel atoms is reduced, lowering the deuterium ion (and electron) particle source, which has to be compensated by increased fueling [45]. Consequently, if instead of the electron density the deuterium fueling rate is kept at a fixed value (colored lines in figure 8), the upstream separatrix electron density varies considerably (by more than 40 %, see figure 8, right). At higher seeding levels, for which the deuterium fueling rate is high in the feedback cases, the electron density in the feed-forward cases strongly decreases. This also leads to strongly increased temperatures in most regions, which makes a comparison of the different cases difficult. Nevertheless, the impurity density distributions and the divertor enrichment in the feed-forward cases (see figure 9) show the same qualitative behavior as in the feedback cases (figure 7, bottom right), with a clear Ar density redistribution at high seeding levels. Therefore, the variation of the deuterium fueling rate itself cannot be the cause for the density redistribution in the feedback cases.

An investigation of the location of the impurity seeding position revealed that the position does not have a significant impact on the simulation results under the investigated steady state conditions. The standard seeding positions for Ar and N are indicated in figure 1. However, similar results (including the Ar density redistribution) are obtained in simulations in which the impurity gas puff positions are reversed, i.e. N is injected from the midplane and Ar from the PFR. Considering the particle sources in the plasma, this weak impact of the seeding location on the plasma parameters is not surprising. While the impurity gas puff is in the order of $10^{20}\,\mathrm{s}^{-1}$ (in atomic flux), the total recycling rate of the impurities at the walls, mainly at the divertor targets, is usually in the order of $10^{22}\,\mathrm{s}^{-1}$ or even higher. Therefore, recycling is by far the strongest particle source in the plasma, whereas the gas puff and its position are mostly irrelevant (as soon as the total impurity content is saturated, i.e. under steady state conditions). However, it should be noted, that in the N seeding cases this situation might change if a more realistic surface model is applied, instead of the assumption of full recycling.

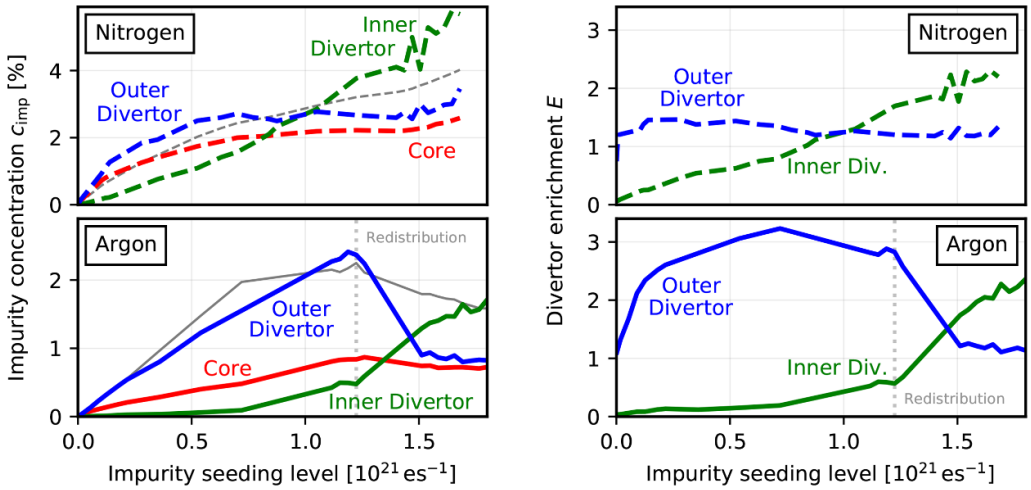

Figure 7. Impurity concentrations c_{imp} in different regions (left) and inner and outer divertor enrichment $E := \frac{c_{\mathrm{imp,div}}}{c_{\mathrm{imp,core}}}$ (right) for N (top) and Ar (bottom). Additionally, the ratio of the impurity seeding to the deuterium fueling rate $\frac{\Gamma_{\mathrm{imp}}}{\Gamma_{\mathrm{D}+}+\Gamma_{\mathrm{imp}}}$ is shown (thin gray lines), which is often used in the experiment to estimate the impurity concentration.

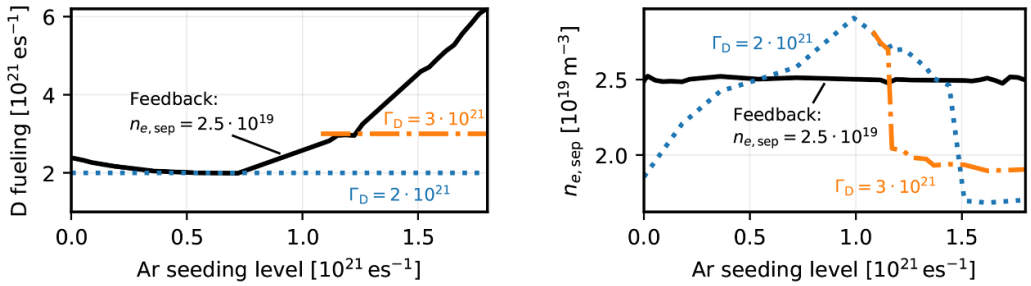

Figure 8. Left: Required deuterium fueling rate to sustain an electron density at the outer midplane separatrix of $n_{\mathrm{e,sep}} = 2.5 \cdot 10^{19}\,\mathrm{m}^{-3}$ in the Ar seeding scan (solid black line). For a comparison two additional Ar seeding scans with constant deuterium fueling rates of $\Gamma_{\mathrm{D}} = 2 \cdot 10^{21}\,\mathrm{es}^{-1}$ and $3 \cdot 10^{21}\,\mathrm{es}^{-1}$ have been performed (colored lines). Right: The corresponding electron density at the outer midplane separatrix.

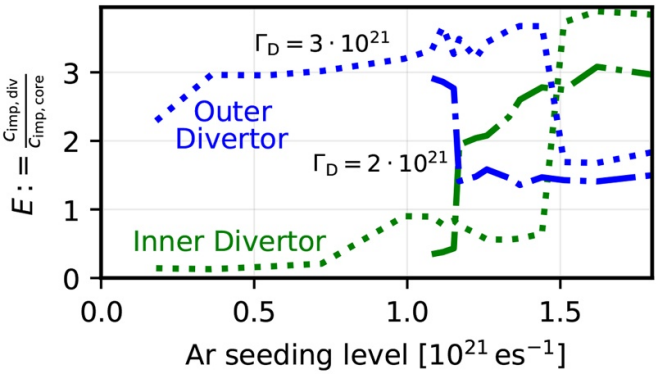

Figure 9. Inner and outer divertor enrichment plotted for the Ar seeding scans with constant deuterium fueling rates ($\Gamma_{\mathrm{D}} = 2 \cdot 10^{21}\,\mathrm{s}^{-1}$ and $3 \cdot 10^{21}\,\mathrm{s}^{-1}$). The same qualitative behavior as in the feedback cases with the Ar density redistribution can be observed (cf figure 7, bottom right).

2.3. *Impurity transport*

In general, the particle density of a certain particle species in a certain region is determined by the particle sources and sinks and the divergence of the flux. Usually, the strongest particle source in the different plasma regions is the ionization of neutral atoms. These either come directly from the gas puff, from volume recombination, or from recycling at the vessel walls, mostly at the divertor targets. For impurities, the volume recombination rate is negligibly low, around $10^{9}\,\mathrm{s}^{-1}$ at seeding levels in the order of $10^{20}\,\mathrm{s}^{-1}$ (in atomic flux). On the other hand, the recycling rate (under the assumption of full recycling) is typically in the order of $10^{22}\,\mathrm{s}^{-1}$, and therefore, the dominant contribution. For the redistribution of particle densities—as observed in the previous section—the neutral fluxes might play an important role, as the neutrals are not necessarily immediately ionized and can travel across different plasma regions, independently of the magnetic field lines. The role of the neutral and ion fluxes in establishing a certain impurity density distribution is discussed in the following.

To investigate the importance of the neutral impurity fluxes (of Ar and N atoms, as well as N_2 molecules), figure 10 shows the fluxes across different test surfaces (positions indicated in the small overlaid plot). For both Ar and N the neutral fluxes through the PFR (black lines) are always directed from the HFS to the LFS, but small, i.e. below $0.25 \cdot 10^{20}\,\mathrm{s}^{-1}$ for N and below $0.1 \cdot 10^{20}\,\mathrm{s}^{-1}$ for Ar. Due to the strongly rising (neutral)

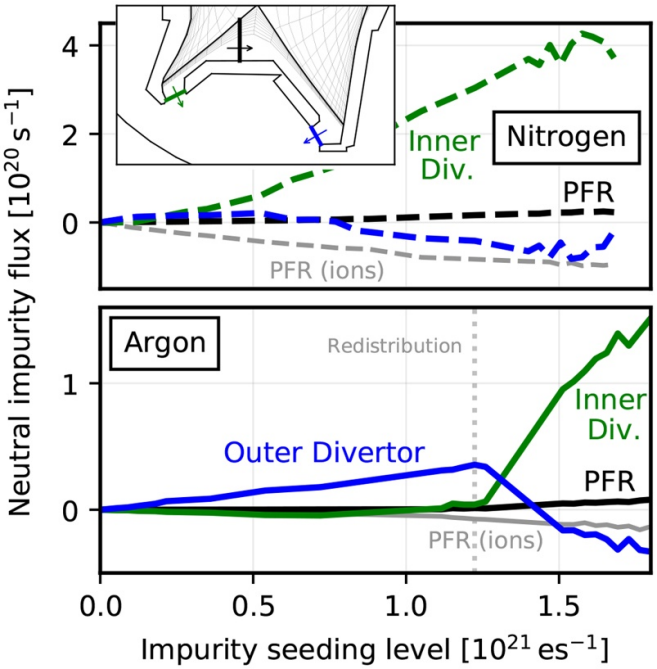

Figure 10. Neutral Ar and N fluxes (also considering N_2 molecules) from the HFS PFR to the LFS PFR (black), and towards the subdivertor region from the inner/outer divertor region (green/blue), i.e. across the surfaces displayed in the overlaid plot (with arrows indicating the positive flow direction). For comparison, the gray lines show the parallel impurity ion flux through the PFR (negative values towards the HFS).

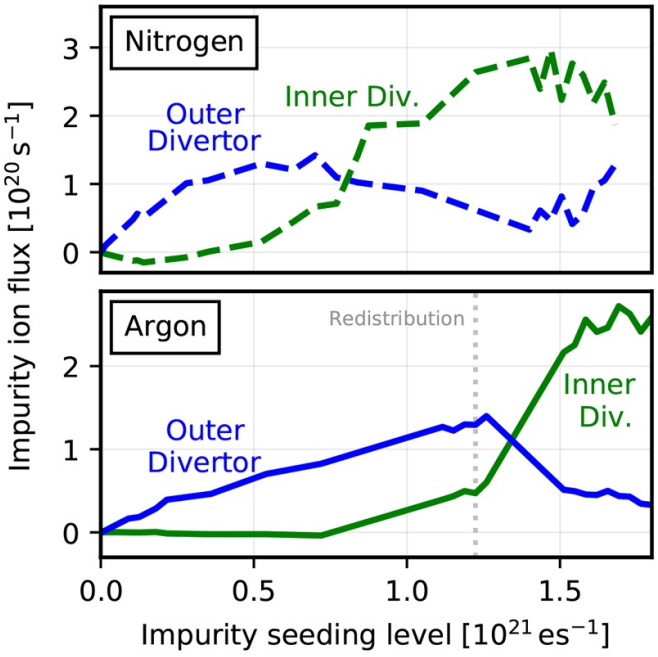

Figure 11. Total parallel impurity ion fluxes entering the inner and outer divertor regions through the divertor entrance from the main chamber SOL.

impurity densities in the inner divertor (cf figure 3), a large amount of neutrals (up to $4 \cdot 10^{20}\,\mathrm{s}^{-1}$ for N and $1.5 \cdot 10^{20}\,\mathrm{s}^{-1}$ for Ar) escape from the divertor towards the subdivertor region as the impurity seeding level is increased. At low seeding levels also the outer divertor loses neutrals to the subdivertor. However, at high seeding levels neutrals enter the outer divertor coming from the subdivertor region (see figure 10, negative values of blue lines). This can be interpreted as a neutral particle flux from the inner to the outer divertor through the subdivertor region. Therefore, the neutral fluxes do not explain the modified Ar density distribution from the LFS to the HFS at high seeding levels. Instead, the neutrals rather counteract the redistribution, and balance the increasing parallel impurity ion flux going from the LFS to the HFS through the PFR (see figure 10, gray lines) and via the main chamber SOL.

Figure 11 shows the net parallel ion influx of impurities into the inner and outer divertor regions coming from the main chamber SOL. The flux enters the divertor volume through the divertor entrance, poloidally at the position of the X-point (see figure 1, transition between yellow and blue/green). The high flux values of up to $3 \cdot 10^{20}\,\mathrm{s}^{-1}$ exceeding the applied impurity seeding level (up to $10^{20}\,\mathrm{s}^{-1}$ for Ar and $2.6 \cdot 10^{20}\,\mathrm{s}^{-1}$ for N, in atomic fluxes) are sustained by ionization sources in the main chamber SOL, mainly from recycling. Figure 12 schematically shows the typical particle flow patterns in the SOL for a case at low seeding and high seeding as they are observed for both, impurities and main ions. The corresponding normalized Ar flux in the numerical grid of the SOLPS 5.0 simulations is

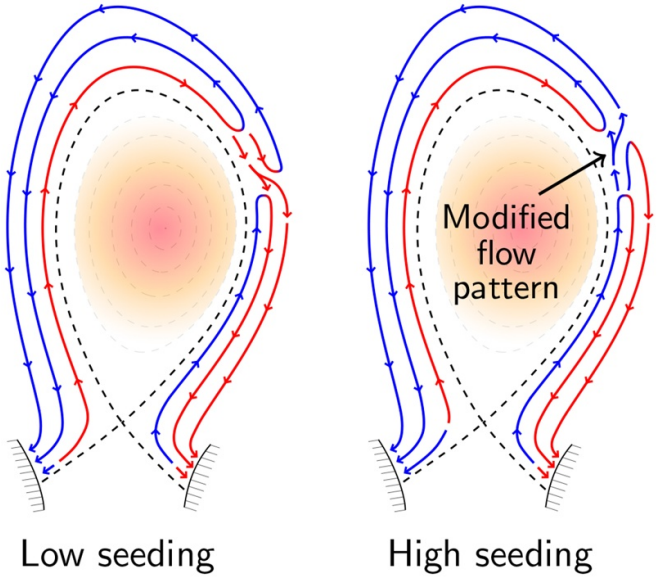

Figure 12. Schematic drawing of the typical particle flux patterns (of both, impurities and main ions) as they are observed in the SOLPS 5.0 simulations at low and high impurity seeding levels.

shown in figure 13. The general main ion and impurity flow direction in most of the SOL is not affected by the impurity seeding (see figure 12). However, the actual particle flux (i.e. the amount of particles per second), and more importantly, around the outer midplane position also the qualitative flow patterns (figure 12 and figure 13), do change significantly. At low seeding levels most particles within the SOL are directed towards the outer divertor. Particles escaping the outer divertor in the near SOL cannot reach beyond the outer midplane, as the

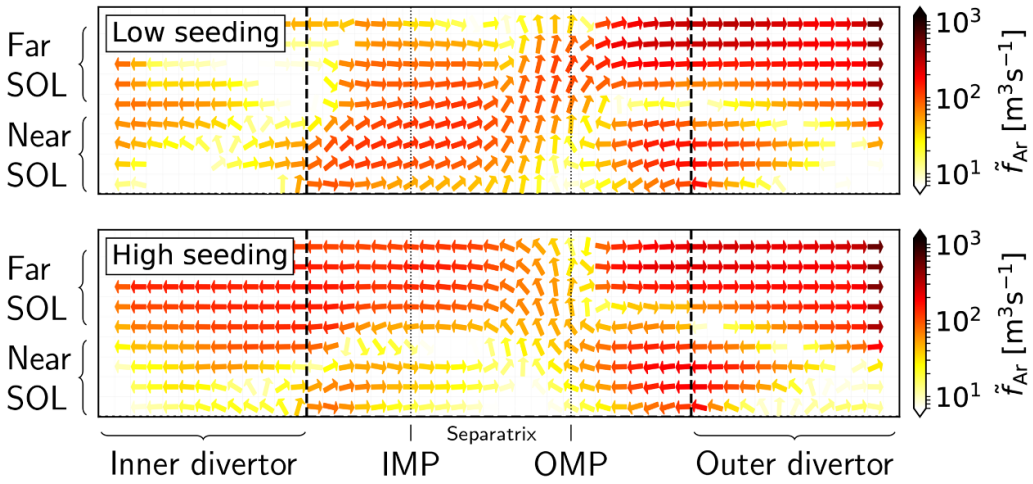

Figure 13. Ar particle flux (summed over all charge states and normalized by the Ar density) in the SOL for a case at low ($\Gamma_{Ar} = 0.36 \cdot 10^{21}\,\mathrm{es}^{-1}$) and high seeding level ($\Gamma_{Ar} = 1.51 \cdot 10^{21}\,\mathrm{es}^{-1}$) plotted in the SOLPS 5.0 numerical grid.

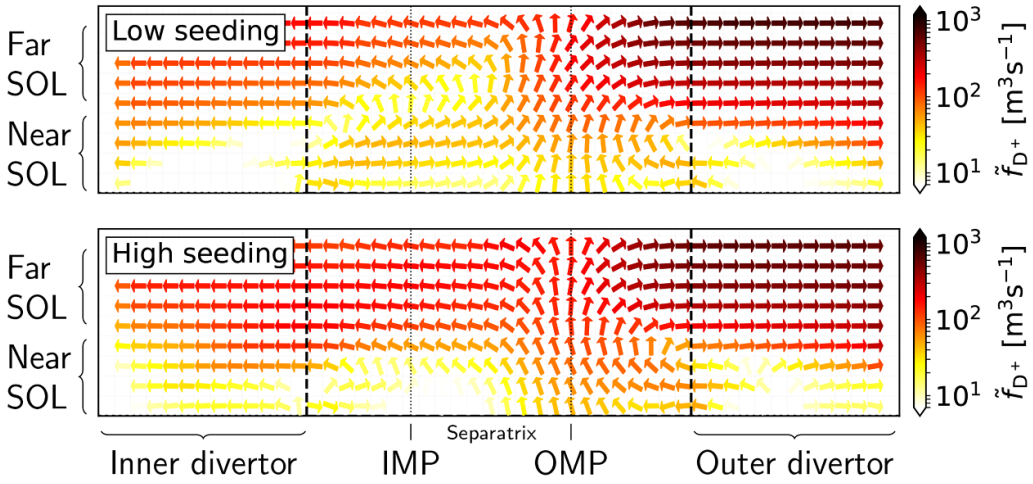

Figure 14. Main ion particle flux (normalized by the main ion density) in the SOL for a case at low ($\Gamma_{Ar} = 0.36 \cdot 10^{21}\,\mathrm{es}^{-1}$) and high Ar seeding level ($\Gamma_{Ar} = 1.51 \cdot 10^{21}\,\mathrm{es}^{-1}$) plotted in the SOLPS 5.0 numerical grid.

flux is reversed at this position. Therefore, at low seeding level, effectively no impurity ion can move from the outer divertor to the inner divertor through the SOL. However, at high seeding level, the behavior changes and only a small fraction of particles is returned to the outer divertor, while the majority flows towards the inner divertor. In this situation impurity ions cannot move from the inner to the outer divertor along the SOL.

To understand the impurity flows in the SOL, the forces in the plasma have to be investigated [46–49]. The most important force acting on the impurities is the friction force $F_{fr} \propto Z^2(u_{D^+} - u_{imp})$ determined by the main ion plasma flow u_{D^+}. If no other forces were present, F_{fr} would equilibrate the velocities of impurities and main ions, until as a result F_{fr} vanishes. Therefore, the main ion plasma flow determines the baseline of the impurity flow. A deviation of the impurity flow from this baseline is mainly due to the thermal force $F_{th} \propto Z^2 \nabla T$ caused by temperature gradients ∇T. Additional pressure gradient forces and electrostatic forces are small in the main chamber SOL, and even though they become stronger closer to the targets, they do not turn out to be relevant for the explanation of the impurity density redistribution and the divertor retention.

As it can be seen by a comparison of figure 13 with figure 14, showing the normalized impurity and main ion flows in the SOL, the main cause for the inversion of the impurity flow is a modification of the main ion or background flow patterns. These background flow patterns are determined by the deuterium ionization sources which are shown in figure 15 (left) for the Ar and N seeding scans in the inner and outer divertor. Due to the changing temperatures and densities, the deuterium ionization is strongly affected by the impurity seeding. The main ion flows entering the inner and outer divertor regions through the divertor entrance (figure 15, right) are inverted as soon as the ionization source in the inner divertor drops below the source in the outer divertor (causing the qualitative change of the particle flow patterns, cf figures 12–14). According to F_{fr} this background flow inversion also redistributes the impurities from the outer to the inner divertor.

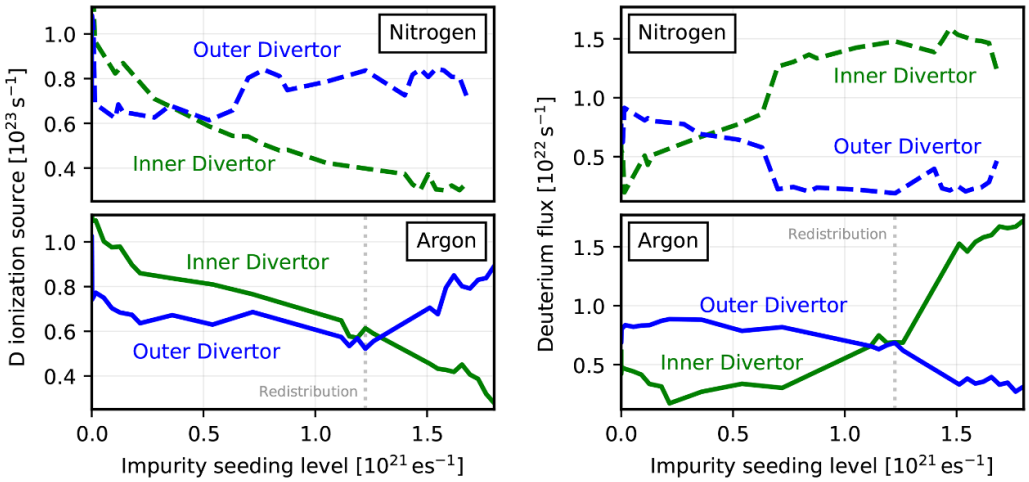

Figure 15. Left: Total deuterium ionization source in the inner and outer divertor region for the N (top) and Ar (bottom) seeding scan. Right: Parallel D^+ ion fluxes entering the inner and outer divertor regions.

Comparing N and Ar it can be observed that due to the different radiation efficiency N has a stronger impact on the temperature (and therefore also on the main ion ionization source) in the colder inner divertor and a less strong impact in the hotter outer divertor (cf figure 4). Consequently, with N seeding the deuterium ionization in the inner divertor drops below the ionization rate in the outer divertor already at relatively low seeding levels (figure 15, top left). As at this point the N content is still relatively low, the inversion of the N concentration (and enrichment) only occurs as a smooth transition (see figure 7 around $\Gamma_N = 0.9 \cdot 10^{21}\,\mathrm{es}^{-1}$). In contrast, for Ar the redistribution appears at relatively high seeding levels. At this point, with the high Ar content, the impact of the impurities on the plasma is strongly affected by the impurity density redistribution, resulting in a further reduction (increase) of the temperature and the deuterium ionization rate in the inner (outer) divertor. Therefore, the flow inversion becomes a self-enhancing process, which explains the sudden change of the flow patterns and the strong and pronounced Ar density redistribution.

Additionally, the modification of the impurity flow pattern is enhanced by the thermal force F_{th} acting on the impurities (resulting in a more pronounced effect in figure 13 compared to figure 14). Due to the parallel temperature profile, which is peaked around the outer midplane position (OMP), F_{th} ($\propto \nabla T$) drags particles away from the targets towards the OMP. However, with increasing seeding level and changing temperature, F_{th} becomes weaker on the HFS, while on the LFS it becomes stronger, resulting in an enhanced drag of particles towards the inner divertor. This can be seen in figure 16 (left) showing F_{th} and F_{fr} acting on the Ar impurities along a flux tube in the near SOL for three different cases with low ($\Gamma_{\mathrm{Ar}} = 0.36 \cdot 10^{21}\,\mathrm{es}^{-1}$), medium ($1.12 \cdot 10^{21}\,\mathrm{es}^{-1}$) and high Ar seeding level ($1.51 \cdot 10^{21}\,\mathrm{es}^{-1}$). As F_{th} results in a deviation of the impurity flow from the background plasma flow, it directly results in an equivalent counteractive friction force $F_{\mathrm{fr}} \approx -F_{\mathrm{th}}$, and therefore, the forces are usually well balanced in the steady state simulations. On the right hand side of figure 16, the total Ar particle flux in the entire SOL (i.e. summed over all Ar charge states and all flux tubes within the SOL) is plotted for the three cases. The Ar flux towards the inner target increases considerably with increasing seeding level (e.g. at the inner divertor entrance from $\sim 0\,\mathrm{s}^{-1}$ to $5 \cdot 10^{19}\,\mathrm{s}^{-1}$ to $23 \cdot 10^{19}\,\mathrm{s}^{-1}$), which is both due to the modified background plasma flow and the enhanced F_{th}.

2.4. Outer divertor impurity retention

A detailed review on previous publications on the impurity transport in the divertor and the impurity retention can be found, e.g. in [50], and references therein. The role of the relative positions of the impurity ionization front and the impurity stagnation point is presented in [36]. In the following the impact of the impurity seeding on the divertor retention, and especially on the stagnation point position is analyzed, according to the SOLPS 5.0 simulations and a simplified semi-analytic model.

A typical Ar impurity flux pattern in the outer divertor is depicted in figure 17 for a case at medium seeding level ($\Gamma_{\mathrm{Ar}} = 1.12 \cdot 10^{21}\,\mathrm{es}^{-1}$). Qualitatively, similar impurity flux patterns are also observed at different seeding levels, both for N and Ar. While in the far SOL the impurities flow towards the target plate, in the near SOL the impurity flux is reversed at the stagnation point, beyond which particles stream out of the divertor region. The contributions of different charge states to the Ar impurity flux across the outer divertor entrance are depicted in figure 18 for all SOL flux tubes. The escaping particle flux in the near SOL mostly consists of charge states from Ar^{5+} to Ar^{8+}. In the N seeding case (not shown here) the same is true for N^{3+} to N^{5+}.

The impurity ion flux onto the divertor target is recycled, which results in a strong neutral particle source at the target plate. The recycled impurity neutrals are able to move upstream towards the stagnation point only as long as they are not ionized, since as ions they would adapt to the plasma flow and stream back towards the target plate. Only if the

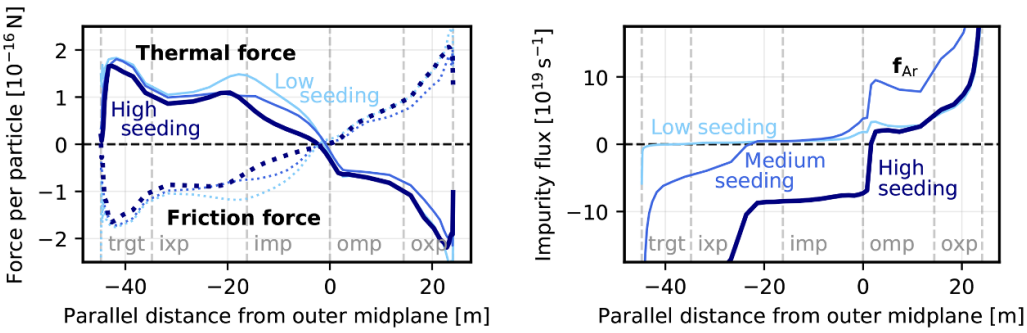

Figure 16. Left: Parallel thermal and friction forces acting on a single Ar particle (averaged over all charge states) plotted along a flux tube in the near SOL (at $\Delta s_{\mathrm{omp}} \approx 1.5$ mm distance from the separatrix at the OMP) for a case at low, medium and high Ar seeding. Right: Total Ar particle flux (i.e. sum over all charge states and flux tubes) in the whole SOL. Negative values are directed towards the inner, positive values towards the outer target. The vertical dashed lines mark the inner target, inner X-point, inner midplane, outer midplane, outer X-point and outer target positions.

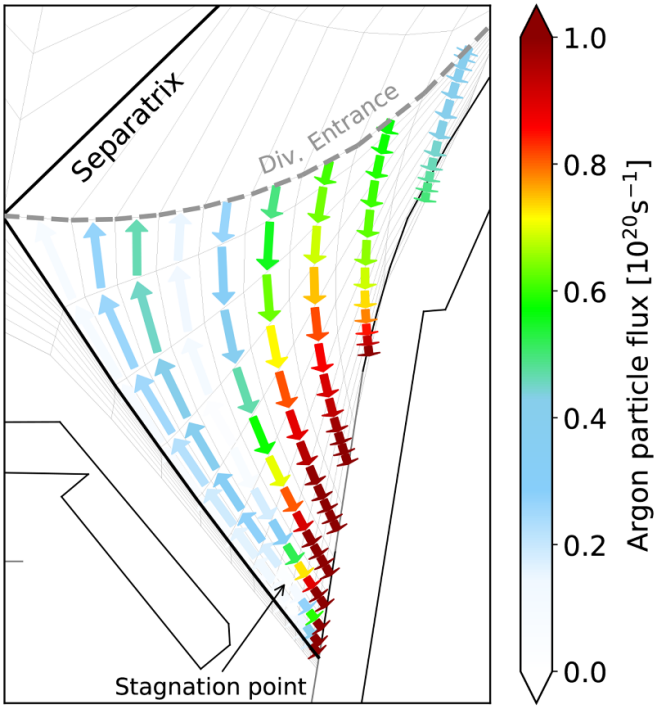

Figure 17. Typical Ar impurity flux pattern in the outer divertor for a case at medium seeding level ($\Gamma_{\mathrm{Ar}} = 1.12 \cdot 10^{21}\,\mathrm{es}^{-1}$).

ionization occurs beyond the impurity stagnation point the ionized particles stream out of the divertor region. Therefore, the divertor impurity retention is determined by the relative positions of the neutral impurity ionization front and the impurity stagnation point [36]. A longer ionization mean free path of the impurity neutrals results in increased divertor leakage. The simulations yield an average ionization mean free path in the outer divertor region (including the PFR) of roughly 6 cm for Ar and 9 cm for N. Hence, the shorter ionization mean free path of Ar explains its superior divertor enrichment, while the stronger N divertor leakage, even at low seeding levels, accounts for the smooth and less pronounced impurity density redistribution for N. It should be noted, that due to a very short N_2 dissociation mean free path (in the order of only a few micrometers in the simulations), N_2 is almost immediately dissociated, and identical results are observed in simulations with atomic N seeding and molecular N_2 seeding.

The impact of the impurity seeding on the divertor retention is schematically illustrated in figure 19. With increasing impurity seeding and decreasing temperatures the ionization front is shifted away from the target (going from dashed to solid lines in figure 19), according to the ionization potential of the particles. This leads to an increasing fraction of neutral impurity atoms that are able to reach beyond the impurity stagnation point, which contributes to a reduced divertor retention. On the other hand, the impurity seeding also has an impact on the thermal and friction forces (determined by the temperature gradient and the main ion plasma flow), which determine the impurity stagnation point position.

In the converged steady state case all forces acting on the impurity ions are balanced. As the only relevant forces in the present simulations are F_{th} and F_{fr} we can write (for each impurity charge state separately) [46–49]:

$$F_{\mathrm{th}} \approx -F_{\mathrm{fr}} = -c_{\mathrm{fr}}\left(u_{\mathrm{D}^+} - u_{\mathrm{imp}}\right) \tag{2}$$

$$\Rightarrow \quad u_{\mathrm{imp}} \approx u_{\mathrm{D}^+} + F_{\mathrm{th}}/c_{\mathrm{fr}} \tag{3}$$

with the friction coefficient c_{fr} and the parallel velocities of the main ions and impurities u_{D^+} and u_{imp}. The impurity stagnation point (i.e. $u_{\mathrm{imp}} = 0$) is at the position where the background plasma flow is compensated by the ratio of the thermal force and the friction coefficient:

$$u_{\mathrm{D}^+} = -F_{\mathrm{th}}/c_{\mathrm{fr}}. \tag{4}$$

These terms are shown in figure 20 exemplary for Ar^{6+} in a case at high seeding level ($\Gamma_{\mathrm{Ar}} = 1.51 \cdot 10^{21}\,\mathrm{es}^{-1}$), plotted against the parallel distance from the outer divertor target. The strong impact of the thermal force can only persist because of a reduction of the friction coefficient c_{fr} in regions with higher temperature, i.e. further away from the target (see figure 20, right). According to [47], this is expected as the

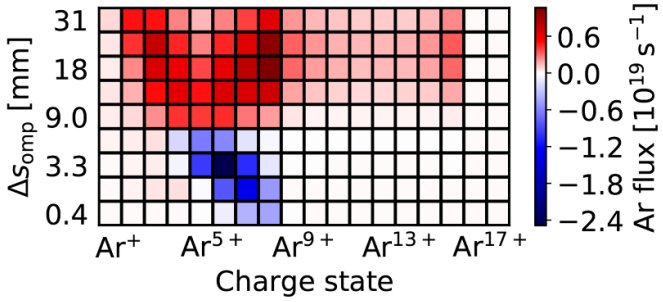

Figure 18. Ar particle flux across the outer divertor entrance (i.e. across the dashed gray line in figure 17) plotted separately for different flux tubes (i.e. different distances from the separatrix at the OMP Δs_{omp}) and for all Ar charge states for a case at medium seeding level ($\Gamma_{Ar} = 1.12 \cdot 10^{21}\,es^{-1}$). The negative values (blue) in the near SOL represent an outflux of particles from the divertor region.

friction coefficient is inversely proportional to the temperature: $c_{fr} \propto n_D Z^2/T^{3/2}$. With $F_{th} \propto Z^2 \cdot \nabla T$, we obtain

$$F_{th}/c_{fr} \propto \frac{T^{3/2} \cdot \nabla T}{n_D}, \tag{5}$$

where n_D is the main ion density and T is the ion temperature. Considering the impact of impurity seeding on the plasma, we expect decreasing temperature in the divertor region (and usually also increasing density, unless there is significant pressure loss). Under these conditions, impurity seeding results in a reduction of F_{th}/c_{fr}, which causes a shift of the impurity stagnation point towards the main ion stagnation point and, therefore, further away from the target (which is confirmed by the simulations). Disregarding the simultaneously shifted neutral ionization front position of the impurities, this indicates a reduced amount of particles reaching beyond the impurity stagnation point, and therefore, an increased divertor impurity retention at higher seeding levels. However, in the overall picture, this mechanism is in competition with the reduced divertor retention caused by the shifted neutral ionization front position, as it was described above.

To investigate under which conditions which of these two mechanisms dominates, the stagnation point position was calculated (according to the above equations and references [46–49]) for various different combinations of parameters in a simplified semi-analytic model. Based on the simulation results, the assumptions of this simplified model are the following:

- Linearly increasing temperatures ($T := T_e = T_i$) with increasing distance from the target (i.e. a constant temperature gradient ∇T, and therefore, constant F_{th}),
- either a constant plasma density n throughout the whole divertor region, or a constant pressure p, resulting in $n = p/T$,
- linearly decreasing velocity of the main ion plasma flow u_{D^+} with increasing distance from the target (either with a fixed velocity at the target $u_{D^+,trgt}$, or deduced as the sound speed $u_{D^+,trgt} = c_s = \sqrt{k_B T/m_{D^+}}$).

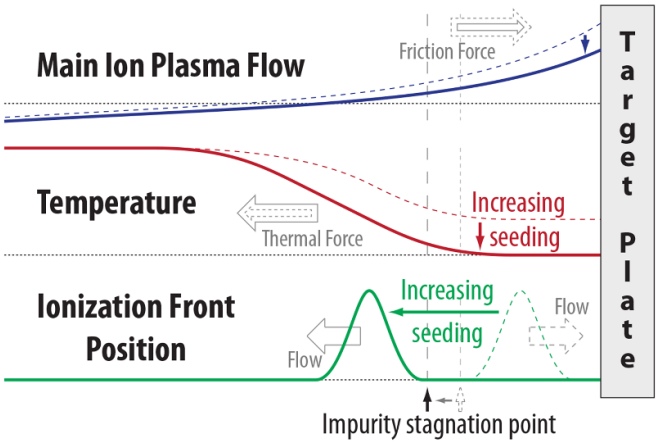

Figure 19. Schematic impact of reduced target temperatures and shifted ionization front positions on the divertor impurity retention. For clarity the shift of the ionization front position is strongly exaggerated.

Table 1. Summary of the results from the simplified model, showing the parameter dependence of the stagnation point position and of the temperature at the stagnation point. The arrows indicate if the stagnation point position is shifted away from the target (←|) or towards the target (→|), and if it is shifted to higher (↗) or lower (↘) temperatures, as the corresponding parameter in the first column is increased.

Increasing input parameter	Stagnation point position	Temperature at stagn. point
Target temperature T_{trgt}	⇄|	↗
Temperature gradient ∇T	→|	↑↓
Main ion target velocity $u_{D^+,trgt}$	←|	↗
Main ion velocity gradient ∇u_{D^+}	→|	↘
Plasma density n	←|	↗
Plasma pressure p	←|	↗
Impurity mass m_{imp}	→|	↘

With these simplifications, the system can be described by a small number of input parameters (see table 1, left column). The shift of the stagnation point position under a variation of the input parameters of the model was calculated for a set of more than 400.000 different parameter combinations. In table 1 the results of this analysis are summarized. The arrows in the middle column of the table indicate whether the stagnation point is shifted away from the target (←|) or towards the target (→|) as the parameter in the first column is increased (while all other parameters are kept fixed). For the impact of the target temperature on the stagnation point position, the behavior depends on the remaining parameters (indicated by the '⇄|' symbol), if $u_{D^+,trgt} = c_s$. Otherwise, with a fixed $u_{D^+,trgt}$, the stagnation point is always shifted away from the target with decreasing target temperatures T_{trgt}, as discussed above. At high impurity masses m_{imp}, the stagnation point is independent of m_{imp}, and only at low masses it moves away from the target with decreasing m_{imp} due to a $(1 + m_D/m_{imp})$ term in the friction coefficient. This indicates a better divertor retention for light impurities (under the assumption of an identical ionization mean free path of the

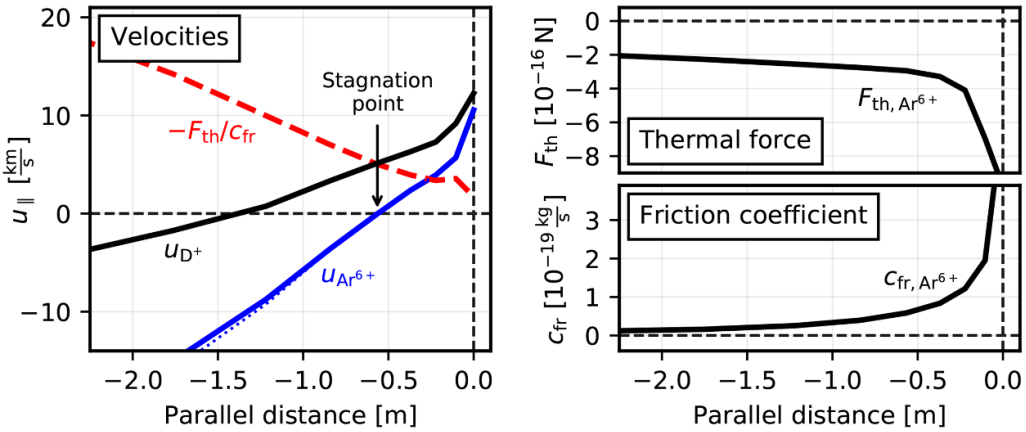

Figure 20. Left: Parallel velocities of the main ions u_{D^+} and Ar^{6+} impurities $u_{Ar^{6+}}$ plotted against the distance from the outer target (in the near SOL, $\Delta s_{omp} \approx 1.5$ mm, for a case at high seeding level, $\Gamma_{Ar} = 1.51 \cdot 10^{21}\,es^{-1}$). Additionally, the ratio of the thermal force and the friction coefficient $-F_{th}/c_{fr}$ is shown, which determines the impurity stagnation point position. Right: Thermal force F_{th} and friction coefficient c_{fr} plotted separately (both for Ar^{6+}).

neutral impurity atoms). According to this factor, the friction coefficient for N is about 9 % larger than that for Ar, which already has a small but noticeable impact on the stagnation point position (with the absolute impact depending on the various parameters in the model). However, the reader should be reminded, that with the longer ionization mean free path of N, N still shows a stronger divertor leakage than Ar.

To be able to correlate the shift of the impurity stagnation point with the shift of the impurity ionization front, one can investigate the parameter dependence of the temperature at the stagnation point, as the temperature largely determines the ionization front position. This is shown in the third column of table 1. For enhanced divertor retention, the impurity stagnation point should be at a position with high temperature. In this case many impurity neutrals are already ionized before they can reach beyond the stagnation point, and therefore, the particles stay confined in the divertor region. The crucial result from the simplified model is that with decreasing target temperatures (i.e. with increasing impurity seeding), the impurity stagnation point is always shifted to lower temperatures in all investigated cases. This indicates that despite the shifted stagnation point position, the dominant mechanism is expected to be the shift of the neutral impurity ionization front, which results in a reduction of the divertor impurity retention with increasing seeding levels. This is a critical conclusion, making it even more challenging to find an optimum impurity seeding recipe to overcome the power exhaust problem.

3. Discussion

Impurity seeding will be an important prerequisite for a safe operation of future fusion devices. A valuable tool to study impurity seeded plasmas is provided by the SOLPS 5.0 code. However, the simulations have several limitations and constraints which should be considered when it comes to interpretation.

A comparison of simulations with atomic N seeding and molecular N_2 seeding revealed identical results. Additional surface interactions and molecular effects like ammonia production, which might result in additional power loss due to the impurities, are not taken into account. These effects are an open area of research [51–53] and not topic of this contribution (as they are also not provided in the atomic reaction database used in this work [54]). Also the disputable assumption of fully recycling N at the boundaries of the computational grid has to be considered. With a more realistic surface model, higher N seeding levels might be required to obtain similar radiation fractions, due to wall pumping of N. Regarding the neutral divertor pressure, it should be noted, that there is a discrepancy between experiment and simulation [55]. This issue can only be resolved with activated drift terms and modified SOL transport [56], which is not attempted in this work. In the present simulations, the neutral divertor pressure is in the order of only 0.1 Pa, which results in reduced neutral pumping and particle throughput. This explains why the fueling and seeding rates in the simulations do not resemble the experimentally applied values at similar plasma conditions.

Another limitation of the code is the purely diffusive approach of the perpendicular transport with fixed transport coefficients. With increasing seeding levels (for both Ar and N) a slight decrease of the radial fall-off length of the upstream density and power flux is observed. Fortunately, the deviations are small ($\lambda_{n_e} \approx 16 \pm 2$ mm and $\lambda_q \approx 1.9 \pm 0.3$ mm), and therefore, the comparability of the different simulations is not expected to be affected significantly by the impurity seeding.

Without neo-classical effects and due to the lack of ELMs [57] and ELM-flushing [58], some of the most important mechanisms for the core impurity accumulation are not accounted for. Consequently, the impurity concentrations and enrichment values do not necessarily agree with experimental values. Furthermore, in a future fusion device the pedestal and edge impurity transport is expected to differ from the transport in a smaller machine like ASDEX Upgrade [59]. Without the

consideration of ELMs also the impact of impurity seeding on the ELM size (and therefore also on the target erosion), which might be beneficial [17], was not studied in this work.

One of the most important limitations of the simulations in this work is the missing impact of fluid drifts on the simulation results. Due to numerical instabilities, the activation of drift terms in SOLPS proves to be a difficult and protracted task. Code development progress and advances in the numerical treatment improved the situation in the newer SOLPS-ITER code version [60, 61], and results of first SOLPS-ITER drift cases are already being published (e.g. [36, 62]). However, for the present contribution (using SOLPS 5.0) no converged drift cases could be obtained so far. The impact of drifts has been investigated thoroughly, both in experiment and simulations [36, 56, 63–66]. It is commonly observed, that drifts enhance the asymmetry between the inner and outer target temperature, i.e. drifts contribute to higher (lower) temperatures at the outer (inner) target. Increased ion fluxes at the inner target (unless detachment sets in) and reduced fluxes at the outer target are reported. The drifts also lead to parallel Pfirsch-Schlüter flows [67] and shift particles (both main ions and impurities) in the common SOL towards the outer divertor. This will have an impact on the main ion and impurity particle flow patterns in the SOL (see figures 13 and 14), that were identified to be crucial for the explanation of the impurity density redistribution in the non-drift simulations discussed in this work. With an increased temperature at the outer target, also the reduction of the outer divertor retention, as discussed in section 2.4, might be mitigated. Therefore, it can be assumed, that with drifts the Ar density redistribution will be mitigated or shifted to higher impurity seeding levels.

The constraints of the simulations have to be kept in mind. Nevertheless, the physics understanding gained by the analysis is fundamentally valid and the impact of additional mechanisms (like drifts) can only be understood in its entirety if the situation without these additional mechanisms is well-understood. The observed differences between the impact of Ar and N on the plasma in the SOLPS 5.0 simulations agree well with the observations reported in [6]. For an experimental analysis of mixed Ar and N impurities on ASDEX Upgrade, dedicated discharges have been performed recently. Preliminary analysis of the discharges confirms, that the impact of the impurities on the plasma, and the radiation distribution can be affected by an adjustment of the impurity mixture. Regarding the impurity transport, the observed flow patterns (of both main ions and impurities, cf figure 12) slightly differ from the flows observed in [36], which most probably can be attributed to the impact of drifts. Attempts to experimentally assess the divertor retention are, e.g. reported in [7, 8]. In [7] at higher densities an improved divertor retention is observed, while after detachment the divertor retention decreased. This is consistent with the expectations from the simplified semi-analytic model described in section 2.4. On the other hand, in [8], a reduced divertor retention with increasing divertor temperature is observed, which contradicts the simplified model. Possibly, this might be explained by a modified main ion plasma flow due to the higher heating power applied at higher divertor temperatures in [8].

4. Summary

A detailed analysis of SOLPS 5.0 simulations with Ar and N seeding on the basis of ASDEX Upgrade H-mode plasmas has been performed. The impact of the impurity seeding on the plasma background was self-consistently taken into account. In the simulations Ar shows high divertor enrichment for low to medium seeding seeding levels (i.e. below $\Gamma_{\mathrm{Ar}} \approx 1.22 \cdot 10^{21} \frac{e}{s}$). However, it also reveals a detrimental impact on the pedestal top temperature which is not observed with N seeding at comparable divertor conditions (i.e. at similar target temperatures and peak power loads). This can be explained by the high Ar radiation efficiency, especially in the core region. On the other hand, N leads to a stronger fuel dilution, which also needs to be limited in a future tokamak, as it reduces the maximum achievable fusion rate. A trade-off between pedestal top temperature drop and fuel dilution can be achieved by mixing both impurities.

For the analysis of impurity transport it was shown that impurity seeding has a strong impact on the main ion ionization sources in the divertor regions. Above a certain impurity seeding level, this results in an inverted main ion background flow in the main chamber SOL, especially around the outer midplane position, which also strongly affects the impurity flow patterns. As this causes the impurities to be redistributed from the outer to the inner divertor, their impact on the main ion ionization sources increases further, resulting in a self-enhancing process. Additionally, the inversion of the impurity flow patterns is enhanced by increasing thermal forces in the main chamber SOL.

According to a simplified semi-analytic model, the present work revealed, that with a reduction of the target temperature (e.g. induced by increasing impurity seeding), both the ionization front of the neutral impurities, as well as the impurity stagnation point position are shifted away from the target. This implies, that there is a competition between both mechanisms, which is shown to result in a reduced divertor retention at lower divertor temperatures in all investigated cases.

With the impurity flow inversion in the main chamber SOL and the reduced outer divertor impurity retention at higher seeding levels, it is possible to explain the observed Ar density redistribution (where Ar impurities are redistributed from the outer to the inner divertor as a certain seeding level is exceeded). For N this density redistribution is observed to be much less pronounced. On the one hand, this is due the different N radiation efficiency, which, compared to Ar, results in a stronger impact of the N impurities on the colder inner divertor and a weaker impact in the hotter outer divertor, and therefore, induces a less pronounced background plasma flow inversion. On the other hand, the longer ionization mean free path of neutral N results in a stronger N divertor leakage, already at low seeding levels, which also accounts for a less abrupt density redistribution.

Acknowledgments

This work has been carried out within the framework of the EUROfusion Consortium and has received funding from the Euratom research and training program 2014–2018 and 2019–2020 under grant agreement No 633053. The views and opinions expressed herein do not necessarily reflect those of the European Commission.

ORCID iD

F Hitzler https://orcid.org/0000-0001-7259-5726

References

[1] Naujoks D *et al* 1996 Tungsten as target material in fusion devices *Nucl. Fusion* **36** 671–87
[2] Loarte A *et al* 2007 *Nucl. Fusion* **47** S203–S263
[3] Pitts R A *et al* 2011 Physics basis and design of the iter plasma-facing components *J. Nucl. Mater.* **415** S957–S964
[4] Wischmeier M 2015 High density operation for reactor-relevant power exhaust *J. Nucl. Mater.* **463** 22–9
[5] Gunn J P *et al* 2017 Surface heat loads on the iter divertor vertical targets *Nucl. Fusion* **57** 046025
[6] Kallenbach A *et al* 2013 Impurity seeding for tokamak power exhaust: from present devices via iter to demo *Plasma Phys. Control. Fusion* **55** 124041
[7] McCracken G M *et al* 1995 Impurity transport in the divertor of the alcator c-mod tokamak *J. Nucl. Mater.* **220–222** 264–8
[8] Roth J, Krieger K and Fussmann G 1992 Divertor retention for recycling impurities *Nucl. Fusion* **32** 1835-44
[9] Goetz J A *et al* 1999 High confinement dissipative divertor operation on alcator c-mod *Phys. Plasmas* **6** 1899-906
[10] Kubo H *et al* 2003 Radiation enhancement and impurity behavior in jt-60u reversed shear discharges *J. Nucl. Mater.* **313–316** 1197–201
[11] Monier-Garbet P *et al* 2005 Impurity-seeded elmy h-modes in jet, with high density and reduced heat load *Nucl. Fusion* **45** 1404–10
[12] Petrie T W *et al* 2007 Compatibility of the radiating divertor with high performance plasmas in diii-d *J. Nucl. Mater.* **363–365** 416–20
[13] Petrie T W *et al* 2009 Impurity behaviour under puff-and-pump radiating divertor conditions *Nucl. Fusion* **49** 065013
[14] Giroud C *et al* 2012 Integration of a radiative divertor for heat load control into jet high triangularity elmy h-mode plasmas *Nucl. Fusion* **52** 063022
[15] Giroud C *et al* 2013 Impact of nitrogen seeding on confinement and power load control of a high-triangularity jet elmy h-mode plasma with a metal wall *Nucl. Fusion* **53** 113025
[16] Potzel S *et al* 2015 Formation of the high density front in the inner far sol at asdex upgrade and jet *J. Nucl. Mater.* **463** 541–5
[17] Reimold F *et al* 2015 Divertor studies in nitrogen induced completely detached h-modes in full tungsten asdex upgrade *Nucl. Fusion* **55** 033004
[18] Guillemaut C *et al* 2017 Real-time control of divertor detachment in h-mode with impurity seeding using langmuir probe feedback in jet-iter-like wall *Plasma Phys. Control. Fusion* **59** 045001
[19] Bernert M *et al* 2017 Power exhaust by sol and pedestal radiation at asdex upgrade and jet *Nuclear Mater. Energy* **12** 111–18
[20] Brunner D *et al* 2017 Surface heat flux feedback controlled impurity seeding experiments with alcator c-mod's high-z vertical target plate divertor: performance, limitations and implications for fusion power reactors *Nucl. Fusion* **57** 086030
[21] Dunne M G 2017 Impact of impurity seeding and divertor conditions on transitions, pedestal structure and elms *Nucl. Fusion* **57** 025002
[22] Glöggler S *et al* 2019 Characterisation of highly radiating neon seeded plasmas in jet-ilw *Nucl. Fusion* **59** 126031
[23] Kallenbach A *et al* 2010 Divertor power load feedback with nitrogen seeding in asdex upgrade *Plasma Phys. Control. Fusion* **52** 055002
[24] Summers H P 2004 *The Adas User Manual*
[25] Pütterich T *et al* 2019 Determination of the tolerable impurity concentrations in a fusion reactor using a consistent set of cooling factors *Nucl. Fusion* **59** 056013
[26] Carolan P G and Piotrowicz V A 1983 The behaviour of impurities out of coronal equilibrium *Plasma Phys.* 25 1065–86
[27] Siccinio M, Fable E, Angioni C, Saarelma S, Scarabosio A and Zohm H 2018 Impact of an integrated core/sol description on the r and bt optimization of tokamak fusion reactors *Nucl. Fusion* **58** 016032
[28] Zohm H *et al* 2013 On the physics guidelines for a tokamak demo *Nucl. Fusion* **53** 073019
[29] Henderson S S *et al* 2018 Determination of volumetric plasma parameters from spectroscopic n ii and n iii line ratio measurements in the asdex upgrade divertor *Nucl. Fusion* **58** 016047
[30] McDermott R M *et al* 2018 Evaluation of impurity densities from charge exchange recombination spectroscopy measurements at asdex upgrade *Plasma Phys. Control. Fusion* **60** 095007
[31] Kallenbach A *et al* 2019 Neutral pressure and separatrix density related models for seed impurity divertor radiation in asdex upgrade *Nuclear Mater. Energy* **18** 166–74
[32] Järvinen A *et al* 2013 Simulations of tungsten transport in the edge of jet elmy h-mode plasmas *J. Nucl. Mater.* **438** S1005–S1009
[33] Islam M S, Nakashima Y and Hatayama A 2017 Investigation of plasma behavior during noble gas injection in the end-cell of gamma 10/pdx by using the multi-fluid code 'linda' *Plasma Phys. Control. Fusion* **59** 125010
[34] Liu X J, Deng G Z, Wang L, Liu S C, Zhang L, Li G Q and Gao X 2017 Modeling study of radiation characteristics with different impurity species seeding in east *Phys. Plasmas* **24** 122509
[35] Xiang L, Wischmeier M, Coster D, Bernert M, Guo H, Luo G and the ASDEX Upgrade 2017 Team Modeling of argon seeding in asdex upgrade h-mode plasma with solps5.0 *Nuclear Mater. Energy* **12** 1146–51
[36] Senichenkov I Y 2019 On mechanisms of impurity leakage and retention in the tokamak divertor *Plasma Phys. Control. Fusion* **61** 045013
[37] Hailong D *et al* 2020 Exploring sf- in-out asymmetry and detachment bifurcation in hl-2m with exb by solps *Nuclear Mater. Energy* **22** 100719
[38] Pan O, Lunt T, Wischmeier M, Coster D and Stroth U 2020 Solps-iter modeling with activated drifts for a snowflake divertor in asdex upgrade *Plasma Phys. Control. Fusion* **62** 045004
[39] Chen Z P, Kotschenreuther M, Mahajan S M and Roeltgen J 2020 Solps-iter modeling of boosted carbon radiation through non-coronal effects in an x-divertor facilitating detachment in diii-d *Nucl. Fusion* **60** 046005

[40] Sytova E *et al* 2019 Comparing n versus ne as divertor radiators in asdex-upgrade and iter *Nuclear Mater. Energy* **19** 72–8
[41] Yamoto S, Hoshino K, Homma Y, Nakano T and Hayashi N 2020 Simulation study of mixed-impurity seeding with extension of integrated divertor code sonic *Plasma Phys. Control. Fusion* **62** 045006
[42] Schneider R *et al* 2006 Plasma edge physics with b2-eirene *Contrib. Plasma Phys.* **46** 3–191
[43] Kotov V, Reiter D, Pitts R A, Jachmich S, Huber A and Coster D P 2008 Numerical modelling of high density jet divertor plasma with the solps4.2 (b2-eirene) code *Plasma Phys. Control. Fusion* **50** 105012
[44] Meisl G *et al* 2014 Implantation and erosion of nitrogen in tungsten *New J. Phys.* **16** 093018
[45] Krasheninnikov S I *et al* 2016 Divertor plasma detachment *Phys. Plasmas* **23** 055602
[46] Harbour P J and Morgan J G 1983 The transport of impurity ions in a scrape-off plasma Controlled Fusion and Plasma Physics (Proc. 11th Eur. Conf. Aachen *Part II, European Physical Society* **7D** 427–30 1983
[47] Neuhauser J, Schneider W, Wunderlich R and Lackner K 1984 Modelling of impurity flow in the tokamak scrape-off layer *Nucl. Fusion* **24** 39-47
[48] Stangeby P C and Elder J D 1995 Impurity retention by divertors. i. one dimensional models *Nucl. Fusion* **35** 1391–412
[49] Stangeby P C 2000 *The Plasma Boundary of Magnetic Fusion Devices* (Boca Raton, FL: CRC Press) (https://doi.org/10.1201/9781420033328)
[50] Shimizu K, Takizuka T and Sakasai A 1997 A review on impurity transport in divertors *J. Nucl. Mater.* **241–243** 167–81
[51] Perillo R *et al* 2018 Studying the influence of nitrogen seeding in a detached-like hydrogen plasma by means of numerical simulations *Plasma Phys. Control. Fusion* **60** 105004
[52] Drenik A *et al* 2019 Evolution of nitrogen concentration and ammonia production in n2-seeded h-mode discharges at asdex upgrade *Nucl. Fusion* **59** 046010
[53] Ezumi N *et al* 2019 Synergistic effect of nitrogen and hydrogen seeding gases on plasma detachment in the gamma 10/pdx tandem mirror *Nucl. Fusion* **59** 066030
[54] Reiter D 2011 *The Data File Amjuel:Additional Atomic and Molecular Data for Eirene FZ* (Forschungszentrum Jülich GmbH)
[55] Reimold F *et al* 2015 Experimental studies and modeling of complete h-mode divertor detachment in asdex upgrade *J. Nucl. Mater.* **463** 128–34
[56] Reimold F *et al* 2017 The high field side high density region in solps-modeling of nitrogen-seeded h-modes in asdex upgrade *Nuclear Materials and Energy* **12** 193–9
[57] Zohm H 1996 Edge localized modes (elms) *Plasma Physics and Controled Fusion* **38** 105–28
[58] Pütterich T *et al* 2011 Elm flushing and impurity transport in the h-mode edge barrier in asdex upgrade *J. Nucl. Mater.* **415** 334–9
[59] Dux R *et al* 2014 Transport of tungsten in the h-mode edge transport barrier of iter *Plasma Phys. Control. Fusion* **56** 124003
[60] Wiesen S *et al* 2015 The new solps-iter code package *J. Nucl. Mater.* **463** 480–4
[61] Bonnin X *et al* 2016 Presentation of the new solps-iter code package for tokamak plasma edge modelling *Plasma and Fusion Research* **11** 1403102
[62] Sytova E *et al* 2018 Impact of a new general form of friction and thermal forces on solps-iter modelling results *Contrib. Plasma Phys.* **58** 622–8
[63] Chankin A 1997 Classical drifts in the tokamak sol and divertor: models and experiment *J. Nucl. Mater.* **241–243** 199–213
[64] Asakura N 2007 Understanding the sol flow in l-mode plasma on divertor tokamaks and its influence on the plasma transport *J. Nucl. Mater.* **363–365** 41–51
[65] Chankin A and Coster D 2013 The role of drifts in the plasma transport at the tokamak core–sol interface *J. Nucl. Mater.* **438** S463–S466
[66] Aho-Mantila L *et al* 2017 Assessment of solps5.0 divertor solutions with drifts and currents against l-mode experiments in asdex upgrade and jet *Plasma Phys. Control. Fusion* **59** 035003
[67] Chankin A V *et al* 2001 Interpretation of sol flows and target asymmetries in jet using edge2d code calculations *J. Nucl. Mater.* **290–293** 518–24